

An Improved Inertial Preintegration Model in Factor Graph Optimization for High Accuracy Positioning of Intelligent Vehicles

Liang Zhang¹, Member, IEEE, Weisong Wen¹, Li-Ta Hsu², Senior Member, IEEE, and Tao Zhang¹

Abstract—Accurate and reliable positioning is of great importance for the realization of intelligent vehicles (IV). Factor graph optimization (FGO) has been popularized in the field of robotics for state estimation. As a ubiquitous sensor, the IMU is widely used for vehicular positioning based on the preintegration theory using FGO. However, the existing preintegration model fails to consider the earth's rotation, which challenges the attitude and positioning performance of vehicles equipped with high-precision inertial measurement units (IMU). To fill this gap, an accurate IMU factor that accounts for the earth's rotation rate is designed in this article. First, an exact preintegration measurement model is derived based on a high-precision inertial navigation system (INS) mechanization. The proposed factor is more accurate and it enables the application of the FGO more suitable for inertial-based integrated navigation with different precision IMUs. In both simulation and field tests, the INS/ Global Navigation Satellite System (GNSS) integration, as a representative of inertial-based integrated navigation, is used to verify the performance of the proposed preintegration factor. The navigation results using our experimental car reveal that the proposed model leads to a more accurate estimation, outperforming the traditional preintegration models, especially in the aspect of attitude estimation.

Index Terms—Factor graph optimization, IMU preintegration, inertial navigation, integrated navigation, vehicle navigation.

I. INTRODUCTION

HIGH performance of attitude and positioning is critical for intelligent vehicles (IV) [1], [2]. An inertial navigation system (INS) is a promising sensor as it contains complete

Manuscript received 29 April 2023; revised 16 May 2023 and 27 May 2023; accepted 29 May 2023. Date of publication 8 June 2023; date of current version 23 February 2024. This work was supported in part by Postdoc Matching Fund Scheme W22E, in part by the Fund for Key Laboratory of Inertial Technology 2021-JCJQ-LB-070-05, in part by the Fundamental Research Funds for the Central Universities under Grants 2242023K30005 and 2242023K30006. (*Corresponding author: Weisong Wen*)

Liang Zhang is with the School of Instrument Science Engineering, The Key Laboratory of Micro-Inertial Instrument and Advanced Navigation Technology, Ministry of Education, Southeast University, Nanjing 210096, China (e-mail: liangzhang@seu.edu.cn).

Weisong Wen and Li-Ta Hsu are with the Department of Aeronautical and Aviation Engineering, The Hong Kong Polytechnic University, Hong Kong (e-mail: welson.wen@polyu.edu.hk; lt.hsu@polyu.edu.hk).

Tao Zhang is with the School of Instrument Science and Engineering, The Key Laboratory of Micro-Inertial Instrument and Advanced Navigation Technology, Ministry of Education, Southeast University, Nanjing 210096, China (e-mail: zhangtao22@seu.edu.cn).

Color versions of one or more figures in this article are available at <https://doi.org/10.1109/TIV.2023.3282623>.

Digital Object Identifier 10.1109/TIV.2023.3282623

navigation information, including attitude, velocity, and position [3]. Besides, it has the advantages of fast updating frequency, all-weather operation, and high short-time accuracy. Thus, the inertial-based navigation approach has been widely applied in the field of mobile robotics [4], unmanned aerial vehicles(UAV) [5], and unmanned ground vehicles [6]. However, the errors of INS will accumulate over time [7]. Exploring the suppression approach of inertial navigation errors has always been a research hotspot in the field of autonomous navigation and positioning for IV.

The inertial-based integrated navigation assisted by other sensors is an alternative direction. In particular, a variety of sensors can be integrated with INS for different scenarios. A typical example is an integration of the global navigation satellite system (GNSS) and INS in an open place such as land or air [8]. Especially in intelligent vehicle navigation, INS/GNSS integration is a common way [9], [10]. In particular, the work in [10] proposed to combine the kinematics and dynamics of the vehicles to improve the vehicular navigation accuracy. Besides, light detection and ranging (LiDAR) [11], wheel-odometry [12], and road scene maps [13] are also optional navigation devices in intelligent vehicles. The Kalman filter is an effective method to implement the above integration [14]. In inertial-based integrated navigation, the mechanization of INS is linearized by first-order error expansion in the recursive form. Thus, the Kalman filter based on the error state can achieve satisfactory and efficient state estimation.

A. Related Works

1) *The IMU Preintegration in FGO Becomes Popular:* Different from conventional filtering-based inertial navigation, recent research in simultaneous localization and mapping (SLAM) has shown that the optimization-based method outperforms the filter-based method in terms of estimation accuracy [15]. It takes all the historical states into consideration while the filter-based method only considers the current state and marginalizes all the other previous states. Due to its superior performance, it has attracted more attention in multi-sensor fusion. As early as 2012, factor graph optimization (FGO) has been applied to GNSS positioning [16]. The application of FGO can make GNSS localization more robust and accurate [17], [18], which is critical for intelligent vehicle navigation. With the advent of the preintegration theory [19], FGO is further extended to

inertial-based integrated navigation. Such as the integration of INS and visual [20], LiDAR [21], GNSS [22], and so on. The precision of the IMU factor is crucial for vehicle navigation applying FGO. Otherwise, the performance of inertial-based integrated navigation will degrade. Based on the mechanization of INS in [19], some improved preintegration algorithms have been proposed [23], [24], [25]. However, they cannot meet the accuracy requirement in high precision IMU as the rotational rate of the earth was ignored.

2) *The Existing IMU Preintegration Model has Limitations:* To make the preintegration model more accurate, the rotational rate of the earth is expected to be considered. Thus, a new IMU preintegration with rotating earth is proposed [26]. It is evaluated using the INS/LiDAR integration through an experimental car and confirmed to outperform the traditional preintegration model. In [27], a simple INS/GNSS integrated navigation system is used to verify the accuracy of the Kalman filter and FGO considering the rotating earth. The results confirmed that the FGO can yield the same accuracy as the Kalman filter. However, all of these algorithms are validated through micro-electro-mechanical systems (MEMS) IMU. The performance of FGO will be challenged if a higher precision IMU is used, such as the fiber optic gyroscope (FOG). Considering the coning error under high-rate maneuvering, a preintegration theory based on an equivalent rotation vector is proposed [28]. Recently, an application of FGO on the INS/ultra-short baseline system (USBL) integration demonstrated its usefulness for FOG-based integrated navigation [29]. However, there are still approximate errors in the preintegration model [29], which challenge attitude performance. In short, the existing preintegration schemes have limitations in attitude estimation. Although the rotating earth has been considered in recent research [26], [27], [28], [29], the remaining approximate errors in the model will seriously affect the attitude accuracy. Compared with the high-precision mechanization of INS in the Kalman filter, the inaccuracy of the preintegration model will lead to the attitude accuracy being inferior to that of the Kalman filter. Thus, all these show that in the field of inertial-based high-precision navigation and positioning, FGO still has a certain gap with the Kalman filter. To solve the problems in FGO-based integrated navigation in [27], [29], a more accurate IMU preintegration model is highly expected.

B. Key Contributions of This Article

Not only is positioning accuracy important, but attitude is also important for intelligent vehicles, especially when equipped with high-precision IMUs. To enable the application of the FGO method more suitable for inertial-based integrated navigation with different precision IMUs, an exact residual model and Jacobian matrix of the IMU factor have been re-derived in this article. It can obtain better attitude and positioning performance than the Kalman filter when equipped with high-precision IMU.

The contributions of the article are twofold:

- 1) An accurate IMU residual model considering the rotation earth is rigorously derived, which could be used in the

integrated navigation system based on high-precision IMU for mobile robotics or intelligent vehicles.

- 2) To improve the attitude estimation accuracy of FGO, a prior factor is proposed to suppress the oscillation error of the initial attitude. The proposed model can achieve better attitude performance than that of the traditional preintegration method.

The structure of the article is as follows. The first section is the introduction and includes the current research status. The second section introduces the IMU model and its problem in the traditional preintegration model. The third section derives a new IMU preintegration model. The fourth section verifies the effectiveness of the proposed preintegration model through simulation and field tests. The last section presents a summary.

II. PROBLEM STATEMENT

The coordinate systems are defined first for better comprehension.

- 1) *Body frame (b-frame):* It is an orthogonal reference frame, which is aligned with IMU axes.
- 2) *Navigation frame (n-frame):* It is an orthogonal reference frame, which is aligned with East–North–Up (E-N-U) geodetic axes [30].
- 3) *Earth frame (e-frame):* It is the earth-centered earth-fixed frame (ECEF) [31].
- 4) *World frame (w-frame):* The world frame used in [20] is actually the n-frame at the initial position (n_0 frame) in this article. It is still named w-frame in the article for readability.

The output of IMU can be modeled as follows [32].

$$\begin{aligned}\tilde{\omega}_{ib}^b &= \omega_{ib}^b + \mathbf{b}_g + \mathbf{n}_g \\ \tilde{\mathbf{f}}^b &= \mathbf{f}^b + \mathbf{b}_a + \mathbf{n}_a\end{aligned}\quad (1)$$

where $\tilde{\omega}_{ib}^b$ and $\tilde{\mathbf{f}}^b$ are the actual output of the gyroscopes and accelerometers. ω_{ib}^b and \mathbf{f}^b are the ideal output of IMU. \mathbf{b}_g and \mathbf{b}_a are the bias of the gyroscope and accelerometer. \mathbf{n}_g and \mathbf{n}_a are the white noise, which is assumed to follow a Gaussian distribution as follows.

$$\begin{aligned}\mathbf{n}_g &\sim N(0, \sigma_g^2) \\ \mathbf{n}_a &\sim N(0, \sigma_a^2)\end{aligned}\quad (2)$$

where σ_g^2 and σ_a^2 are the covariance.

In particular, the IMU kinematics used in preintegration can be divided into three types. The first one, which is also most widely used in the field of SLAM systems currently, is as follows [20].

$$\begin{cases} \dot{\mathbf{P}}^w = \mathbf{V}^w \\ \dot{\mathbf{V}}^w = \mathbf{C}_b^w (\tilde{\mathbf{f}}^b - \mathbf{b}_a) + \mathbf{g}^w \\ \dot{\mathbf{C}}_b^w = \mathbf{C}_b^w (\tilde{\omega}_{ib}^b - \mathbf{b}_g) \times \end{cases}\quad (3)$$

where \mathbf{P}^w , \mathbf{V}^w , and \mathbf{C}_b^w denote the position, velocity, and attitude matrix in the w-frame. \mathbf{g}^w is the gravity vector and $(\tilde{\omega}_{ib}^b - \mathbf{b}_g) \times$ denotes the skew matrix.

The disadvantages of this model are obvious. It ignores the rotating earth and the coordinate system is simplified [29]. Thus, it will not be analyzed in this article.

The IMU kinetics model considering the rotating earth has been adopted in preintegration in recent years. Typical is the following [26], [27].

$$\begin{cases} \dot{\mathbf{P}}^w = \mathbf{V}^w \\ \dot{\mathbf{V}}^w = \mathbf{C}_b^w (\tilde{\mathbf{f}}^b - \mathbf{b}_a) + \mathbf{g}^w - 2\omega_{ie}^w \times \mathbf{V}^w \\ \dot{\mathbf{C}}_b^w = \mathbf{C}_b^w (\tilde{\omega}_{wb}^b - \mathbf{b}_g) \times \tilde{\omega}_{wb}^b = \tilde{\omega}_{ib}^b - \mathbf{C}_b^w \omega_{ie}^w \end{cases} \quad (4)$$

where $\omega_{ie}^w = [0 \ \omega_{ie} \cos L \ \omega_{ie} \sin L]^T$. ω_{ie} is the earth's rotation rate.

Another new preintegration model is based on the following IMU kinetics model, where the strap-down inertial navigation propagation equation is defined in n-frame [29].

$$\begin{cases} \dot{\mathbf{C}}_b^n = \mathbf{C}_b^n (\omega_{nb}^b \times) \\ \dot{\mathbf{V}}^n = \mathbf{C}_b^n (\tilde{\mathbf{f}}^b - \mathbf{b}_a) - (2\omega_{ie}^n + \omega_{en}^n) \times \mathbf{V}^n + \mathbf{g}^n \\ \dot{\mathbf{P}}^n = \mathbf{M}_{pv} \mathbf{V}^n \end{cases} \quad (5)$$

where \mathbf{C}_b^n is the rotation matrix from b-frame to n-frame. ω_{nb}^b is defined as follows.

$$\begin{cases} \omega_{nb}^b = \omega_{ib}^b - \mathbf{C}_n^n (\omega_{ie}^n + \omega_{en}^n) \\ \omega_{ie}^n = [0 \ \omega_{ie} \cos L \ \omega_{ie} \sin L]^T \\ \omega_{en}^n = \left[\frac{-V_N}{(R_M+h)} \ \frac{V_E}{R_N+h} \ \frac{V_E \tan L}{R_N+h} \right]^T \end{cases} \quad (6)$$

where ω_{nb}^b is the rotational angular velocity of b frame with respect to n frame. ω_{ie}^n is the rotational angular velocity of e frame with respect to i frame. ω_{en}^n is the rotational angular velocity of n frame with respect to e frame. ω_{ie} is the earth's rotation rate. $\mathbf{V}^n = [V_E \ V_N \ V_U]^T$ is the velocity in the n-frame. R_N , and R_M is the earth parameters [29]. $\mathbf{P}^n = [L \ \lambda \ h]^T$ is the absolute position represented by longitude, latitude and height. \mathbf{M}_{pv} is expressed as follows.

$$\mathbf{M}_{pv} = \begin{bmatrix} 0 & \frac{1}{R_M+h} & 0 \\ \frac{\sec L}{(R_N+h)} & 0 & 0 \\ 0 & 0 & 1 \end{bmatrix} \quad (7)$$

Compared (4) with (5), the IMU kinetics model in (4) is simplified. The centripetal acceleration to the earth caused by the motion of the carrier ($\omega_{en}^n \times \mathbf{V}^n$) is ignored. Thus, the estimation accuracy of preintegration model based on (4) will be inferior to that of the Kalman filter in the condition of high speed and large scale of scenarios.

In (5), it solves the problem of the coordinate system. However, the integration of earth rotation is ignored. The problem of approximate assumption still exists in the preintegration residual model, which will affect the accuracy of attitude heavily. Specifically, the longer the integration period, the lower the attitude accuracy. In addition, the prior factor is not considered in [29], which will make a great shock error of attitude in the initial stage. To solve the problems in the traditional preintegration models, a new IMU preintegration model needs to be designed. According to the analysis of the existing literature, the preintegration model can be divided into three categories. An overview of the

proposed IMU preintegration model along with differences and comparisons with traditional methods is shown in Fig. 1.

In Fig. 1, it can be seen that the proposed method is a further extension of the previous work in [29] to solve the application problem of FGO in high precision inertial based integrated navigation. It can achieve more accurate position and attitude estimation.

III. DESIGN OF NEW IMU PREINTEGRATION MODEL

Firstly, the relationship between preintegration intervals and IMU samples is defined as follows [29].

In Fig. 2, the preintegration interval is from t_i to t_j . The IMU update interval is from t_k to t_{k+1} . In the following article, Δt shares the same meaning as $\Delta t_{k,k+1}$.

The state of the system is defined as follows.

$$\begin{aligned} \mathbf{X} &= [\mathbf{x}_0, \mathbf{x}_1, \mathbf{x}_2, \dots, \mathbf{x}_n]^T \\ \mathbf{x}_i &= [\mathbf{P}_i^n, \mathbf{V}_i^n, \mathbf{C}_{bi}^{ni}, \mathbf{b}_{ai}, \mathbf{b}_{gi}]^T \quad i \in [0, n] \end{aligned} \quad (8)$$

where n is the size of the optimization window.

Based on the above system state, a new IMU factor considering the rotating earth will be derived and detailed in the following.

A. IMU Error Compensation in a Dynamic Environment

The noncommutative error of IMU integration in a dynamic environment will affect the attitude and positioning accuracy. It is important but not considered in the preintegration model like [26].

The output of the gyroscope ($\hat{\omega}_{ib}^b$) after coning error compensation is expressed as [33]:

$$\hat{\omega}_{ib}^b = \left(\Delta \theta_k + \frac{1}{12} \Delta \theta_{k-1} \times \Delta \theta_k \right) / \Delta t \quad (10)$$

where $\Delta \theta_k = \omega_{ib}^b \Delta t$ is the angular increment at epoch k .

The output of the accelerometer ($\hat{\mathbf{f}}^b$) after sculling error compensation is expressed as [34].

$$\hat{\mathbf{f}}^b = \left(\frac{\Delta \mathbf{v}_k + \frac{1}{2} \Delta \theta_k \times \Delta \mathbf{v}_k +}{\frac{1}{12} (\Delta \theta_{k-1} \times \Delta \mathbf{v}_k + \Delta \mathbf{v}_{k-1} \times \Delta \theta_k)} \right) / \Delta t \quad (11)$$

where $\Delta \mathbf{v}_k = \mathbf{f}^b \Delta t$ is the velocity increment at epoch k .

The compensation of coning and sculling errors will improve the performance in a dynamic environment.

B. IMU Residuals

Considering the rotating earth, the attitude residual will be derived firstly. The attitude update equation from epoch $k-1$ to k is as follows.

$$\mathbf{C}_{bk}^{nk} = \mathbf{C}_{nk-1}^{nk} \mathbf{C}_{bk-1}^{nk-1} \mathbf{C}_{bk}^{bk-1} \quad (12)$$

where $\mathbf{C}_{nk-1}^{nk} = \text{Exp}(-\omega_{ink}^{nk} \Delta t)$ and $\mathbf{C}_{bk}^{bk-1} = \text{Exp}(\hat{\omega}_{ibk}^{bk} \Delta t)$. Exp is the exponential map [19]. $\omega_{in}^n = \omega_{ie}^n + \omega_{en}^n$.

Thus, the integration between the preintegration interval can be expressed as follows.

$$\mathbf{C}_{bj}^{nj} = \mathbf{C}_{ni}^{nj} \mathbf{C}_{bi}^{ni} \mathbf{C}_{bj}^{bi} \quad (13)$$

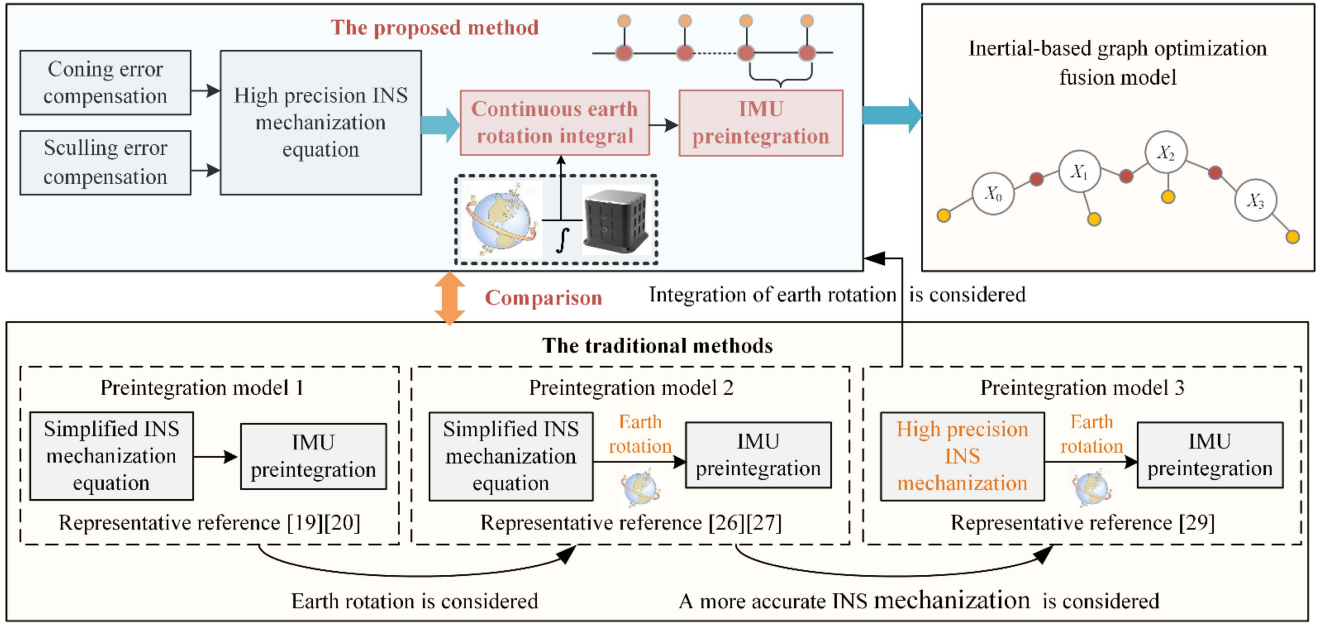


Fig. 1. An overview of the proposed model along with differences and comparisons with traditional methods.

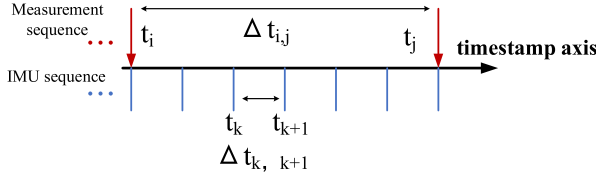


Fig. 2. The relationship between preintegration intervals and IMU samples.

where $\mathbf{C}_{bj}^{bi} = \prod_{k=i}^j \text{Exp}(\hat{\omega}_{ib,k}^b \Delta t)$, $\mathbf{C}_{ni}^{nj} = \prod_{k=i}^j \text{Exp}(-\omega_{ink}^n \Delta t)$.

\mathbf{C}_{bj}^{bi} is the attitude preintegration measurement based on the output of the gyroscope.

Thus, the residual of attitude measurement is as follows.

$$r_{\mathbf{C}_{bj}^{bi}} = \log \left((\mathbf{C}_{bj}^{bi})^T (\mathbf{C}_{ni}^{nj} \mathbf{C}_{bi}^{bi})^T \mathbf{C}_{bj}^{nj} \right) \quad (14)$$

where \log is the logarithm map.

According to (5), the velocity update equation from epoch $k-1$ to k is as follows.

$$\mathbf{V}_k^n = \mathbf{V}_{k-1}^n + \mathbf{C}_{ni}^{nk-1} \mathbf{C}_{bi}^{ni} \mathbf{C}_{bk-1}^{bi} \hat{\mathbf{f}}^{bk-1} \Delta t + \Delta \mathbf{V}_{cor/g(k-1)}^n \quad (15)$$

where $\Delta \mathbf{V}_{cor/g(k)}^n = (\mathbf{g}^n - (2\omega_{ie}^n + \omega_{en}^n) \times \mathbf{V}_{k-1}^n) \Delta t$.

Thus, the integration between the preintegration interval can be expressed as follows.

$$\begin{aligned} \mathbf{V}_j^n &= \mathbf{V}_{j-1}^n + \mathbf{C}_{ni}^{nj-1} \mathbf{C}_{bi}^{ni} \mathbf{C}_{bj-1}^{bi} \hat{\mathbf{f}}^{bj-1} \Delta t + \Delta \mathbf{V}_{cor/g(j-1)}^n \\ &= \mathbf{V}_i^n + \sum_{k=i}^{j-1} \mathbf{C}_{ni}^{nk} \mathbf{C}_{bi}^{ni} \mathbf{C}_{bk}^{bi} \hat{\mathbf{f}}^{bk} \Delta t + \Delta \mathbf{V}_{cor/g(ij)}^n \end{aligned} \quad (16)$$

where $\Delta \mathbf{V}_{cor/g(ij)}^n = (\mathbf{g}^n - (2\omega_{ie}^n + \omega_{en}^n) \times \mathbf{V}_i^n) \Delta t_{i,j}$.

The detailed derivation of (16) can be seen in Appendix A.

According to (16), the $\mathbf{C}_{bk}^{bi} \hat{\mathbf{f}}^{bk} \Delta t$ ($k \in (i, j)$) is the velocity measurement, and the residual of velocity measurement is as follows.

$$r_{\mathbf{V}_{ij}} = \mathbf{V}_j^n - \mathbf{V}_i^n - \sum_{k=i}^{j-1} \mathbf{C}_{ni}^{nk} \mathbf{C}_{bi}^{ni} \mathbf{C}_{bk}^{bi} \hat{\mathbf{f}}^{bk} \Delta t - \Delta \mathbf{V}_{cor/g(ij)}^n \quad (17)$$

In the traditional preintegration model, the velocity update equation is as follows [27], [29].

$$\mathbf{V}_j^n = \mathbf{V}_i^n + \mathbf{C}_{bi}^{mj-1} \sum_{k=i}^{j-1} \mathbf{C}_{bk}^{bi} \hat{\mathbf{f}}^{bk} \Delta t + \Delta \mathbf{V}_{cor/g(ij)}^n \quad (18)$$

In (18), it ignores the changes of \mathbf{C}_{ni}^{nk} and uses \mathbf{C}_{bi}^{mj-1} to replace $\mathbf{C}_{ni}^{nk} \mathbf{C}_{bi}^{ni}$. Thus, the error of the velocity residual will increase with the increase of the integration interval.

According to (5), the position update equation at epoch k is as follows.

$$\mathbf{P}_k^n = \mathbf{P}_{k-1}^n + \mathbf{V}_{k-1}^n \Delta t + \frac{1}{2} \mathbf{C}_{bk-1}^{nk-1} \hat{\mathbf{f}}^{bk-1} \Delta t^2 + \Delta \mathbf{P}_{cor/g(k-1)}^n \quad (19)$$

where $\Delta \mathbf{P}_{cor/g(k-1)}^n = \frac{1}{2} (\mathbf{g}^n - (2\omega_{ie}^n + \omega_{en}^n) \times \mathbf{V}_{k-1}^n) \Delta t^2$.

Thus, the integration between the preintegration interval can be expressed as follows.

$$\begin{aligned} \mathbf{P}_j^n &= \mathbf{P}_i^n + \mathbf{V}_i^n \Delta t_{i,j} + \frac{1}{2} \sum_{k=i}^{j-1} \mathbf{C}_{ni}^{nk} \mathbf{C}_{bi}^{ni} \mathbf{C}_{bk}^{bi} \hat{\mathbf{f}}^{bk} \Delta t^2 \\ &\quad + \sum_{k=i}^{j-2} \mathbf{C}_{ni}^{nk} \mathbf{C}_{bi}^{ni} \mathbf{C}_{bk}^{bi} \hat{\mathbf{f}}^{bk} \Delta t^2 + \Delta \mathbf{P}_{cor/g}^n \end{aligned} \quad (20)$$

where $\Delta \mathbf{P}_{cor/g}^n = \frac{1}{2} (\mathbf{g}^n - (2\omega_{ie}^n + \omega_{en}^n) \times \mathbf{V}_i^n) \Delta t_{i,j}^2$.

The detailed derivation of (20) can be seen in Appendix B.

According to (20), the $\mathbf{C}_{bk}^{bi}\hat{\mathbf{f}}^{bk}\Delta t^2$ ($k \in (i, j)$) is the position measurement and the residual of position measurement is as follows.

$$\begin{aligned} r_{\mathbf{P}_{ij}} &= \mathbf{P}_j^n - \mathbf{P}_i^n - \mathbf{V}_i^n \Delta t_{i,j} - \Delta \mathbf{P}_{cor/g}^n \\ &- \left(\frac{1}{2} \sum_{k=i}^{j-1} \mathbf{C}_{ni}^{nk} \mathbf{C}_{bi}^{ni} \mathbf{C}_{bk}^{bi} \hat{\mathbf{f}}^{bk} \Delta t^2 + \sum_{k=i}^{j-2} \mathbf{C}_{ni}^{nk} \mathbf{C}_{bi}^{ni} \mathbf{C}_{bk}^{bi} \hat{\mathbf{f}}^{bk} \Delta t^2 \right) \end{aligned} \quad (21)$$

In the traditional preintegration model, the position update equation is as follows [27], [29].

$$\begin{aligned} \mathbf{P}_j^n &= \mathbf{P}_i^n + \mathbf{V}_i^n \Delta t_{i,j} + \mathbf{C}_{bi}^{nj} \iint_{t_i}^{t_j} \mathbf{C}_{bt}^{bi} (\tilde{\mathbf{f}}^b - \mathbf{b}_a) dt + \Delta \mathbf{P}_{cor/g}^n \\ &= \mathbf{P}_i^n + \mathbf{V}_i^n \Delta t_{i,j} + \mathbf{C}_{bi}^{nj} \iint_{t_i}^{t_j} \mathbf{C}_{bt}^{bi} (\tilde{\mathbf{f}}^b - \mathbf{b}_a) dt + \Delta \mathbf{P}_{cor/g}^n \end{aligned} \quad (22)$$

Compare (22) with (20), the position integration model has the same problem with that of the velocity integration model as (16) and (18) show. The traditional position integration model is inaccurate either.

C. Incorporating Bias Updates

In Part B, the IMU bias $\tilde{\mathbf{b}}_i = (\tilde{\mathbf{b}}_{ai}, \tilde{\mathbf{b}}_{gi})$ is assumed to be constant over a preintegration period. However, the bias is changed by a small value $\delta \mathbf{b}_i = (\delta \mathbf{b}_{ai}, \delta \mathbf{b}_{gi})$ during the optimization. The estimated bias $\mathbf{b}_i = (\mathbf{b}_{ai}, \mathbf{b}_{gi})$ can be computed as follows.

$$\begin{aligned} \mathbf{b}_{ai} &= \tilde{\mathbf{b}}_{ai} + \delta \mathbf{b}_{ai} \\ \mathbf{b}_{gi} &= \tilde{\mathbf{b}}_{gi} + \delta \mathbf{b}_{gi} \end{aligned} \quad (23)$$

Substitute (23) into the residual equations and update the measurements using the first-order expansion. The attitude residual can be updated as.

$$r_{\mathbf{C}_{bj}^{bi}} = \log \left((\mathbf{C}_{bj}^{bi}(\mathbf{b}_i))^T \left(\mathbf{C}_{ni}^{nj} \mathbf{C}_{bi}^{ni} \right)^T \mathbf{C}_{bj}^{mj} \right) \quad (24)$$

where

$$\mathbf{C}_{bj}^{bi}(\mathbf{b}_i) = \tilde{\mathbf{C}}_{bj}^{bi} \text{Exp} \left(\frac{\partial \tilde{\mathbf{C}}_{bj}^{bi}}{\partial \tilde{\mathbf{b}}_{gi}} \delta \mathbf{b}_{gi} \right) \quad (25)$$

where $\frac{\partial \mathbf{C}_{bj}^{bi}(\tilde{\mathbf{b}}_i)}{\partial \tilde{\mathbf{b}}_{gi}}$ denotes the Jacobian with respect to $\tilde{\mathbf{b}}_{gi}$.

Its detailed expression can be seen in Appendix C. $\tilde{\mathbf{C}}_{bj}^{bi} = \prod_{k=i}^j \text{Exp}(\hat{\omega}_{ibk}^{bk} \Delta t - \tilde{\mathbf{b}}_{gi} \Delta t)$.

The velocity residual can be updated as.

$$\begin{aligned} r_{\mathbf{V}_{ij}} &= \mathbf{V}_j^n - \mathbf{V}_i^n - \Delta \mathbf{V}_{cor/g(ij)}^n \\ &- \sum_{k=i}^{j-1} \mathbf{C}_{ni}^{nk} \mathbf{C}_{bi}^{ni} \tilde{\mathbf{C}}_{bk}^{bi} (\hat{\mathbf{f}}^{bk} - \tilde{\mathbf{b}}_{ai}) \Delta t \\ &- \sum_{k=i}^{j-1} \mathbf{C}_{ni}^{nk} \mathbf{C}_{bi}^{ni} \tilde{\mathbf{C}}_{bk}^{bi} \Delta t \delta \mathbf{b}_{ai} \end{aligned}$$

$$- \sum_{k=i}^{j-1} \mathbf{C}_{ni}^{nk} \mathbf{C}_{bi}^{ni} \tilde{\mathbf{C}}_{bk}^{bi} (\hat{\mathbf{f}}^{bk} - \tilde{\mathbf{b}}_{ai}) \times \frac{\partial \tilde{\mathbf{C}}_{bk}^{bi}}{\partial \tilde{\mathbf{b}}_{gi}} \Delta t \delta \mathbf{b}_{gi} \quad (26)$$

The position residual can be updated as.

$$\begin{aligned} r_{\mathbf{P}_{ij}} &= \mathbf{P}_j^n - \mathbf{P}_i^n - \mathbf{V}_i^n \Delta t_{i,j} - \Delta \mathbf{P}_{cor/g}^n \\ &- \mathbf{L}_1 - \mathbf{L}_2 \delta \mathbf{b}_{ai} - \mathbf{L}_3 \delta \mathbf{b}_{gi} \end{aligned} \quad (27)$$

where

$$\begin{aligned} \mathbf{L}_1 &= \left(\frac{1}{2} \sum_{k=i}^{j-1} \mathbf{C}_{ni}^{nk} \mathbf{C}_{bi}^{ni} \tilde{\mathbf{C}}_{bk}^{bi} (\hat{\mathbf{f}}^{bk} - \tilde{\mathbf{b}}_{ai}) \Delta t^2 \right. \\ &\quad \left. + \sum_{k=i}^{j-2} \mathbf{C}_{ni}^{nk} \mathbf{C}_{bi}^{ni} \tilde{\mathbf{C}}_{bk}^{bi} (\hat{\mathbf{f}}^{bk} - \tilde{\mathbf{b}}_{ai}) \Delta t^2 \right) \\ \mathbf{L}_2 &= \left(\frac{1}{2} \sum_{k=i}^{j-1} \mathbf{C}_{ni}^{nk} \mathbf{C}_{bi}^{ni} \tilde{\mathbf{C}}_{bk}^{bi} \Delta t^2 + \sum_{k=i}^{j-2} \mathbf{C}_{ni}^{nk} \mathbf{C}_{bi}^{ni} \tilde{\mathbf{C}}_{bk}^{bi} \Delta t^2 \right) \\ \mathbf{L}_3 &= \left(\frac{1}{2} \sum_{k=i}^{j-1} \mathbf{C}_{ni}^{nk} \mathbf{C}_{bi}^{ni} \tilde{\mathbf{C}}_{bk}^{bi} (\hat{\mathbf{f}}^{bk} - \tilde{\mathbf{b}}_{ai}) \times \frac{\partial \tilde{\mathbf{C}}_{bk}^{bi}}{\partial \tilde{\mathbf{b}}_{gi}} \Delta t^2 \right. \\ &\quad \left. + \sum_{k=i}^{j-2} \mathbf{C}_{ni}^{nk} \mathbf{C}_{bi}^{ni} \tilde{\mathbf{C}}_{bk}^{bi} (\hat{\mathbf{f}}^{bk} - \tilde{\mathbf{b}}_{ai}) \times \frac{\partial \tilde{\mathbf{C}}_{bk}^{bi}}{\partial \tilde{\mathbf{b}}_{gi}} \Delta t^2 \right) \end{aligned} \quad (28)$$

Thus, the new IMU residual has been derived based on (24), (26), and (28).

The Jacobians of residual errors can be seen in Appendix C.

D. Noise Propagation

The preintegration noise is defined as.

$$\boldsymbol{\eta}_{ij} = [\delta \Phi_{ij}^T \quad \delta \mathbf{v}_{ij}^T \quad \delta \mathbf{p}_{ij}^T \quad \delta \mathbf{b}_a^T \quad \delta \mathbf{b}_g^T]^T \quad (29)$$

Then, the noise propagation can be represented as follows.

$$\boldsymbol{\eta}_{ij} = \mathbf{A}_{j-1} \boldsymbol{\eta}_{ij-1} + \mathbf{B}_{j-1} \boldsymbol{\eta}_{j-1} \quad (30)$$

where $\boldsymbol{\eta}_{j-1} = [\mathbf{n}_a^T \quad \mathbf{n}_g^T]^T$,

$$\begin{aligned} \mathbf{A}_{j-1} &= \begin{bmatrix} \tilde{\mathbf{C}}_{bj-1}^{bj} & 0 & 0 & 0 & -\mathbf{J}_r^{j-1} \Delta t \\ \mathbf{H}_{\mathbf{v}\Phi} & \mathbf{I} & 0 & -\tilde{\mathbf{C}}_{bj-1}^{bj} \Delta t & 0 \\ 0 & \mathbf{I} \Delta t & \mathbf{I} & 0 & 0 \\ 0 & 0 & 0 & \mathbf{I} & 0 \\ 0 & 0 & 0 & 0 & \mathbf{I} \end{bmatrix} \\ \mathbf{B}_{j-1} &= \begin{bmatrix} 0 & \mathbf{J}_r^{j-1} \Delta t \\ \tilde{\mathbf{C}}_{bj-1}^{bj} \Delta t & 0 \\ 0 & 0 \\ 0 & 0 \\ 0 & 0 \end{bmatrix} \end{aligned}$$

where the term $\mathbf{J}_r^{j-1} \doteq \mathbf{J}_r^{j-1}(\hat{\omega}_{ibj-1}^{bj-1} \Delta t - \tilde{\mathbf{b}}_{gi} \Delta t)$ is the right Jacobian of SO(3) [19], [35]. $\mathbf{H}_{\mathbf{v}\Phi} = -\tilde{\mathbf{C}}_{bj-1}^{bj} (\hat{\mathbf{f}}^{bj-1} - \tilde{\mathbf{b}}_{ai}) \times \Delta t$.

Thus, the covariance matrix (Σ_{ij}) of the preintegration measurement noise can be computed as.

$$\Sigma_{ij} = \mathbf{A}_{j-1} \Sigma_{ij-1} \mathbf{A}_{j-1}^T + \mathbf{B}_{j-1} \Sigma_b \mathbf{B}_{j-1}^T \quad (31)$$

where $\Sigma_b = \begin{bmatrix} \sigma_a^2 & 0 \\ 0 & \sigma_g^2 \end{bmatrix}$ is the covariance of IMU noise.

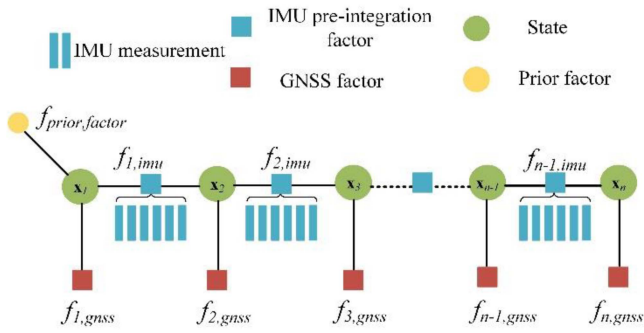


Fig. 3. Graph model of the implemented INS/GNSS integration.

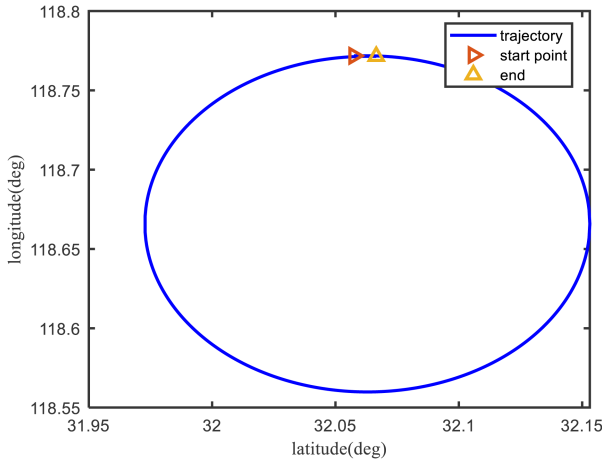


Fig. 4. The simulated trajectory.

IV. EXPERIMENT TEST FOR INS/GNSS INTEGRATION

The INS/GNSS integration, as a representative of inertial-based integrated navigation, is used to verify the performance of FGO using the new preintegration model in this section. A loosely coupled INS/GNSS integration model based on position matching is adopted in the test. The graph model of the integrated navigation system in FGO is as Fig. 3 shows.

The state-of-art preintegration algorithms considering the rotating earth are compared in the article. Symbols used for the experiments are as follows:

KF: Short for the error state-based Kalman filter.

PI1: Short for the preintegration model 1 described in [26]. It is based on the IMU kinetics as (4) shows.

PI2: Short for the preintegration model 2 described in [29]. It is based on the IMU kinetics as (5) shows.

Proposed: The proposed new preintegration model is described in Section III.

A. Simulation Test

As mentioned above, the INS/GNSS integration is adopted to verify the performance of FGO and KF. The simulated trajectory is a circle with a radius of about 10,000 m. The trajectory is as Fig. 4 shows.

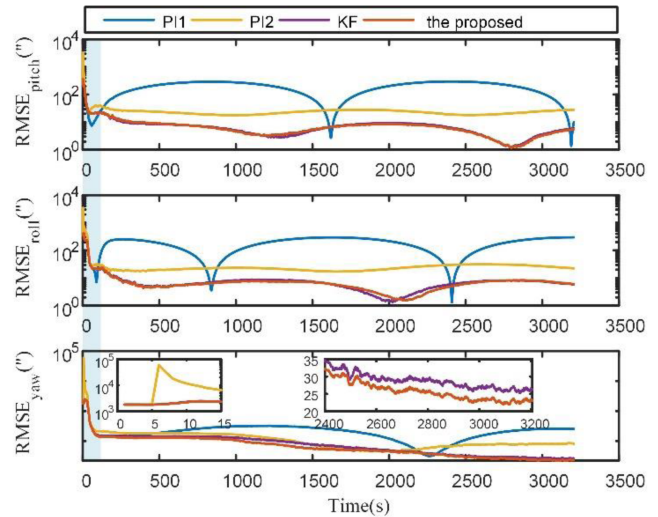


Fig. 5. Comparison of attitude error.

The sensor data is generated according to the trajectory. A navigation-grade IMU is simulated in the test, which includes a triad of gyroscopes (bias $0.01^\circ/h$, random walk $0.001^\circ/\sqrt{h}$) and accelerometer (bias $100 \mu g$, random walk $50 \mu g/\sqrt{Hz}$) [36]. A first-order Markov process is added to the GNSS value. Its correlation time is 3,600 s and standard deviation is 0.1m [37]. Thus, the process noise and measurement noise of Kalman filter are initialized as $\mathbf{Q} = \text{diag}[8.5e-14\mathbf{I}_{1\times 3}, 9.6e-9\mathbf{I}_{1\times 3}]$, $\mathbf{R} = \text{diag}(0.01, 0.01, 0.01)$. The vehicle speed is set as 20 m/s in Fig. 3. The output frequency of GNSS is 1 Hz. The initial navigation parameters are set as follows:

The initial position error: $[1 \quad 1 \quad 3]^T$ m;

The initial velocity error: $[0.1 \quad 0.1 \quad 0.1]^T$ m/s;

The initial attitude error: $[0.1^\circ \quad 0.1^\circ \quad 0.5^\circ]^T$.

To make the results more convincing, 50 independent experiments are conducted in each simulation scenario. Statistics from 50 experiments will be used for comparison. The RMSE of the Monte Carlo simulation test is used as the performance metric. It is defined as follows [38].

$$\text{RMSE}_{pos}(k)$$

$$= \sqrt{1/M \sum_{s=1}^M ((x_k^s - \hat{x}_k^s)^2 + (y_k^s - \hat{y}_k^s)^2 + (z_k^s - \hat{z}_k^s)^2)}$$

$$\text{RMSE}_{\text{roll,pitch or yaw}}(k) = \sqrt{1/M \sum_{s=1}^M (x_k^s - \hat{x}_k^s)^2} \quad (32)$$

where x_k^s is the true value and \hat{x}_k^s is the estimated value at s -th Monte Carlo run at epoch k . x_k^s denotes the value of pitch, roll, or yaw at s -th Monte Carlo run at epoch k .

Thus, the attitude is compared as Fig. 5 shows.

In Fig. 5, PI1 and the proposed method add a prior factor to the graph model. Thus, the initial attitude error changes smoothly. Although the precision of PI2 is better than that of PI1, due to the lack of prior factors, the attitude error of PI2 method oscillates obviously in the initial stage as the blue area shows. Because of

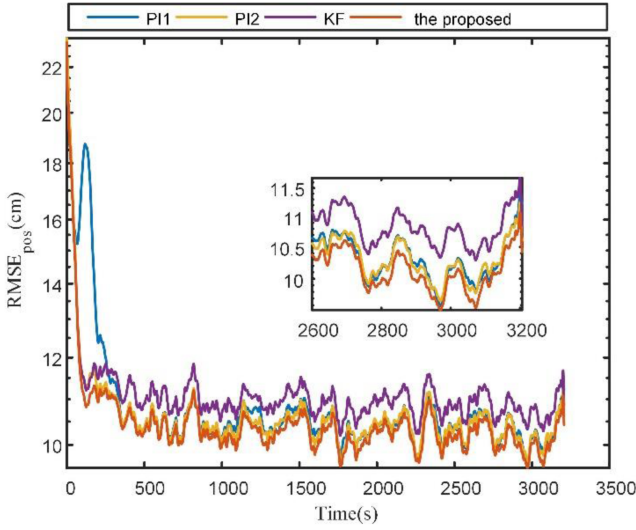


Fig. 6. Comparison of position error.

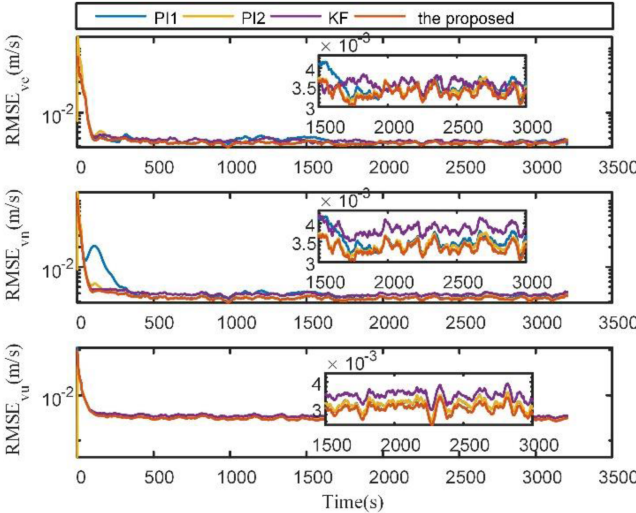


Fig. 7. Comparison of velocity error.

the inaccurate INS mechanization, the roll and pitch errors of the traditional preintegration models (PI1 and PI2) are obviously larger than that of the proposed method and KF method. The proposed method yields the same accuracy as KF. The attitude is observed indirectly. Thus, inaccurate preintegration models will affect attitude accuracy seriously.

The position and velocity errors are compared as Figs. 6 and 7 show.

In Figs. 6 and 7, the position and velocity estimation accuracy based on FGO is better than that of the Kalman filter. Kalman filter is an optimal estimator under the assumption of Gaussian noise. FGO usually has higher estimation accuracy than the Kalman filter in the condition of non-Gaussian noise. Due to the accurate IMU model, the proposed method outperforms the traditional FGO methods in terms of position errors.

The above simulations show that the proposed method have superior performance than the traditional FGO and KF methods in terms of attitude, velocity and position estimation accuracy. To show the superiority of the proposed algorithm in any condition, different simulation scenarios are used to verify the performance of these algorithms in the following.

Test 1. Performance comparison under different GNSS update frequencies: In this test, the influence of update frequency on algorithm performance is compared. The vehicle speed is also set as 20 m/s in Fig. 4. The initial navigation parameters are the same as above. Different measurement period of GNSS is set (5 s, 15 s, 25 s, and 35 s). To analyze the results more quantitatively, the average root-mean-square error (ARMSE) of the Monte Carlo simulation test is used, which is calculated according to the following.

$$\text{RMSE}_m = \sqrt{\frac{1}{N} \sum_{k=1}^N (\hat{x}_k - x_k)^2}$$

$$\text{ARMSE} = \frac{1}{M} \sum_{m=1}^M \text{RMSE}_m \quad (33)$$

where x_k is the true value at epoch i . \hat{x}_k is the estimated value of attitude and position. N is the total number of sampled data and M is the numbers of Monte Carlo simulation test.

Besides, the mean value of the average location error (ALE) is also used as the performance metrics. It is defined as follows.

$$\text{ALE}_m = \frac{1}{N} \sum_{k=1}^N \sqrt{(\hat{x}_k - x_k)^2 + (\hat{y}_k - y_k)^2 + (\hat{z}_k - z_k)^2}$$

$$\text{MALE} = \frac{1}{M} \sum_{m=1}^M \text{ALE}_m \quad (34)$$

where x_k , y_k , and z_k denote the position in the x-axis, y-axis, and z-axis.

Note that the attitude error needs a period of time to converge. Thus, the RMSE of attitude error in the stable phase (1100–3200 s) was calculated. The comparison of attitude error is shown as Fig. 8.

It can be seen from Fig. 8 that the attitude accuracy of PI1 method is the worst. Due to the inaccuracy of the preintegration model in PI2, such as the roll and yaw error, it becomes larger as the period increases. The proposed method always yields the same accuracy as KF or a little bit better.

The comparison of position and velocity error is shown as Figs. 9 and 10.

It can be seen from Figs. 9 and 10 that the position and velocity estimation accuracy of the proposed method outperforms the traditional methods due to the exact preintegration model.

Due to the inaccuracy of the preintegration model, the longer the integration time, the more inaccurate the IMU residual. Thus, the traditional preintegration methods will show bad performance under long time integration. The above simulations confirm that the traditional methods suffer from the influence of integration time. However, the proposed method can hold the estimation accuracy no matter how long the integration time is.

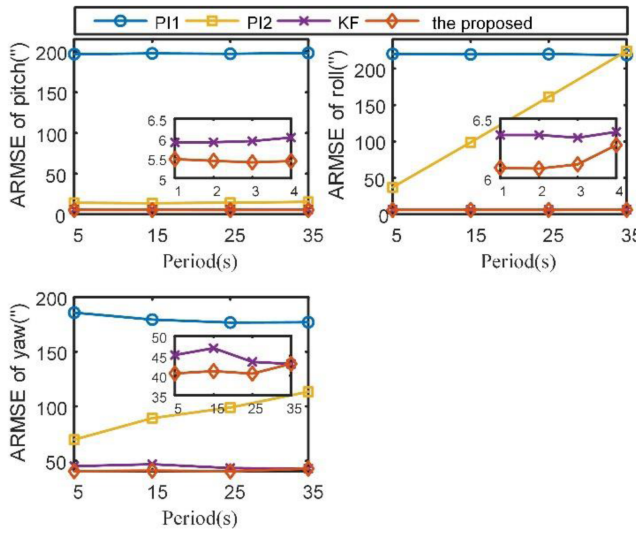


Fig. 8. Comparison of attitude error under different periods.

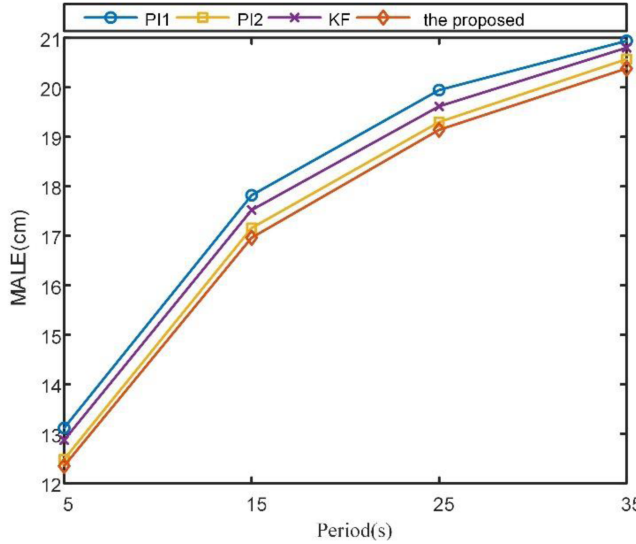


Fig. 9. Comparison of position error under different frequency.

Test 2. Performance comparison under different trajectory radii: The IMU kinetics in (4) is simplified. The preintegration model based on the IMU kinetics in (4) is only suitable for navigation in a small range of scenarios. As the range of motion increases, so does the positioning error. Thus, different trajectory radii are set in this test as Fig. 4 shows. The trajectory radii are set as 1,000 m, 10,000 m, 20,000 m and 30,000 m respectively. Besides, the vehicle speed is also set as 20 m/s. The initial navigation parameters are the same as above. The measurement period of GNSS is set as 5 s. To compare the results more clearly, the difference of ARMSE (DARMSE) and MLE (DMLE) between the traditional methods and the proposed method is used as a performance metric. This means the magnitude of the error relative to the proposed method will be used to indicate the performance. The larger the DARMSE, the worse the performance of the method. If DARMSE is less

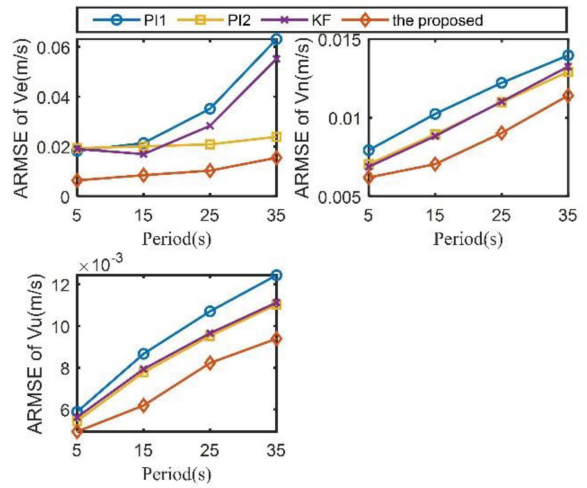


Fig. 10. Comparison of velocity error under different frequency.

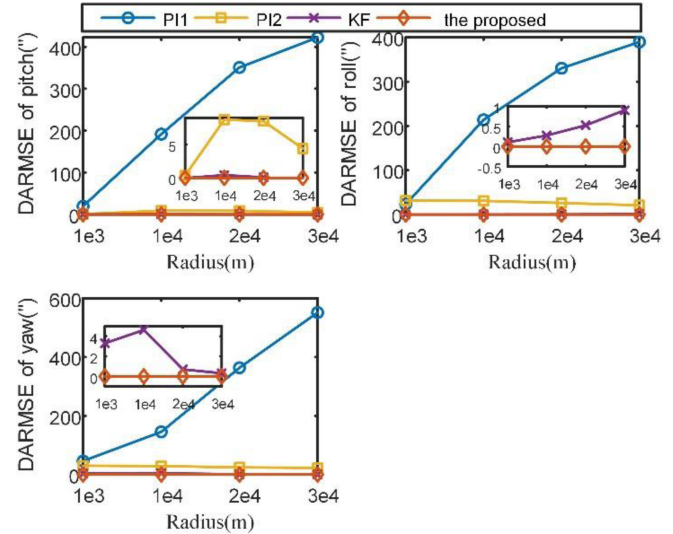


Fig. 11. Comparison of attitude error under different trajectory radii.

than 0, the performance of the method is better than the proposed method.

The comparison of attitude error is shown in Fig. 11.

In Fig. 11, the proposed method indicates a horizontal line at zero. The lines above zero mean a worse performance than the proposed method. It is obvious that the attitude accuracy of PI1 method is the worst. As the range of motion increases, the performance of attitude estimation becomes worse and worse. At the same time, the proposed method always yields the best performance.

The comparison of position and velocity error is shown in Figs. 12 and 13.

In Figs. 12 and 13, the proposed method indicates a horizontal line at zero. The lines above zero mean a worse performance than the proposed method. The positioning accuracy of the PI1 method deteriorates with the increase of radius. Thus, the preintegration model in PI1 is only suitable for navigation

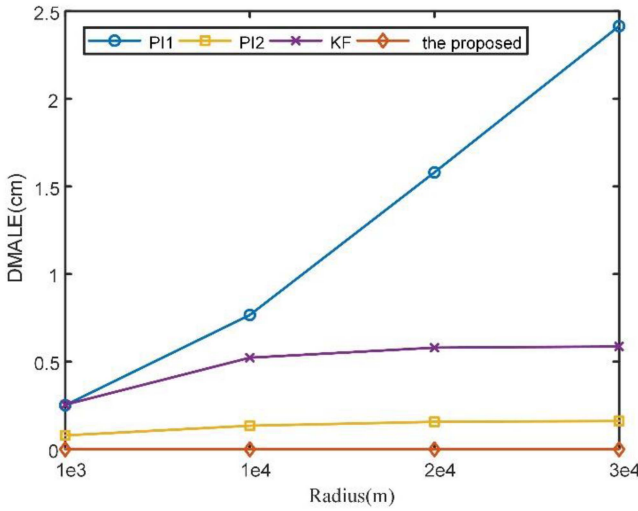


Fig. 12. Comparison of position error under different trajectory radii.

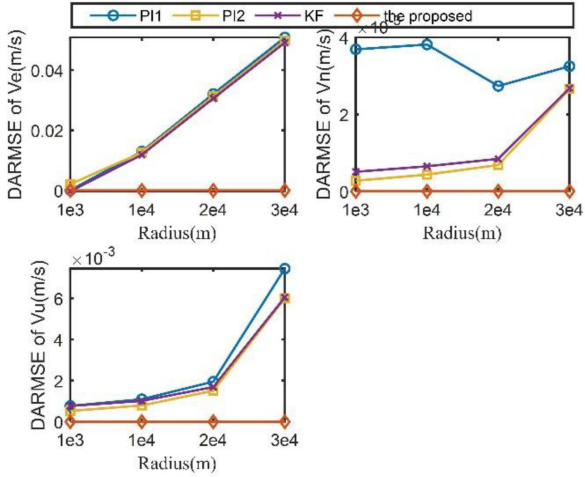


Fig. 13. Comparison of velocity error under different trajectory radii.

in a small range of scenarios. The proposed preintegration model always yields the best performance no matter the motion ranges.

This test confirms that the accuracy of preintegration will affect the positioning accuracy of integrated navigation, especially in the case of a large-scale scenarios. The above experiments confirm that 1) the traditional IMU preintegration model will affect the positioning and attitude accuracy of inertial-based integrated navigation when vehicles are equipped with high-grade IMU. 2) The proposed method is optimal in various environments.

B. Field Test

In the previous subsection, the superiority of the proposed algorithm is proved by simulation experiments. In this subsection, the performance of the FGO method in practical applications will be validated using our experimental car.

The experimental car is equipped with a FOG IMU as Fig. 14 shows. A GNSS antenna is mounted on top of the car, which is



Fig. 14. A schematic of the experimental car.



Fig. 15. Trajectory of the car in google earth.

made by NovAtel. The PHINS, a high-grade navigation system which is made by the iXblue corporation, can output positions and attitudes that we consider as ground truth. The yaw accuracy of PHINS is less than 0.1°secL (L is the latitude of the vehicle). The pitch and roll accuracy of PHINS is less than 0.01° . The bias drift of the gyroscope is $0.02^\circ/\text{h}$ and the angular random walk is $0.005^\circ/\sqrt{\text{h}}$. The bias drift of the accelerometer is $500 \mu\text{g}$ and the random walk is $50 \mu\text{g}/\sqrt{\text{Hz}}$. The output frequency of GNSS and IMU are 1 Hz and 200 Hz respectively.

The trajectory of the car is shown in Fig. 15.

The comparison of position and velocity error is shown in Figs. 16 and 17.

It can be seen from Figs. 16 and 17 that PI1 method performs the worst. As the IMU kinetics is simplified in PI1, its positioning accuracy is inferior to that of PI2 and the proposed method in a dynamic environment. Although an accurate INS mechanization is considered in PI2, the integration of earth rotation is ignored, resulting in the estimation accuracy is less than KF and the proposed method. To analyze the position error quantitatively, RMSE and ALE are used as performance metrics. The statistical results are listed in Table I.

The proposed method yields the best performance among these methods. The position accuracy is improved by 19.8%, and 3.6% respectively compared with the PI1 and PI2 methods in terms of ALE.

The comparison of attitude error is shown in Fig. 18.

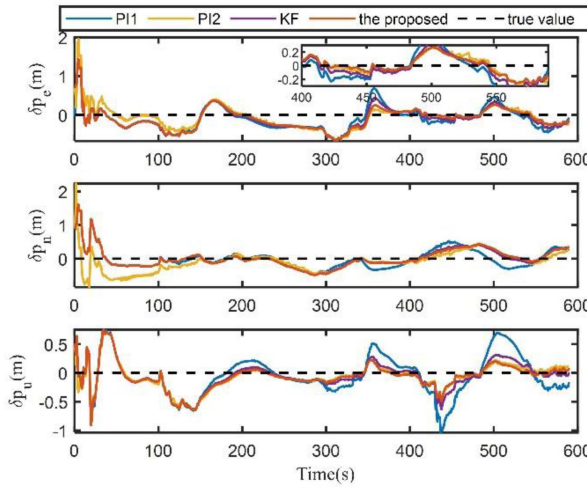


Fig. 16. Comparison of position error in field test.

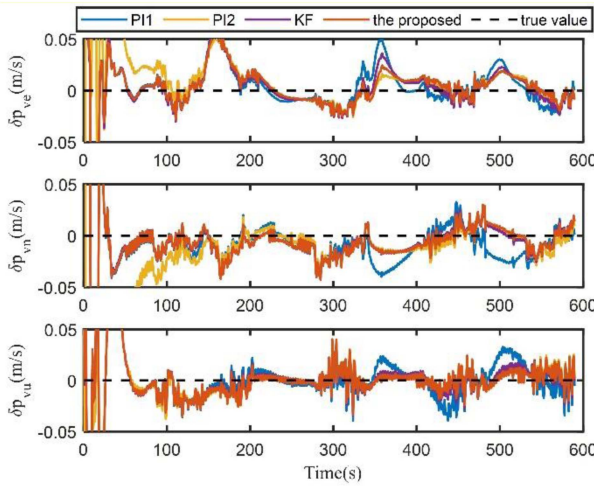


Fig. 17. Comparison of velocity error in field test.

TABLE I
COMPARISON OF POSITIONING ACCURACY IN FIELD TEST

	EPE(m)	NPE(m)	UPE(m)	ALE(m)
PI1	0.313	0.300	0.343	0.484
PI2	0.295	0.299	0.232	0.402
KF	0.299	0.286	0.254	0.413
The Proposed	0.286	0.285	0.230	0.388

In Fig. 18, due to the lack of prior factor, the attitude error of PI2 method oscillates obviously in the initial stage as the blue area shows, which is the same as the simulation results. The proposed method yields comparable attitude accuracy as KF or a little bit better. Due to the exact preintegration model, it outperforms the traditional FGO methods.

The field experiments above verify the effectiveness of the proposed method in practical application. It shows that the proposed preintegration model eliminates the accuracy gap between FGO and KF in terms of applying high-precision IMU.

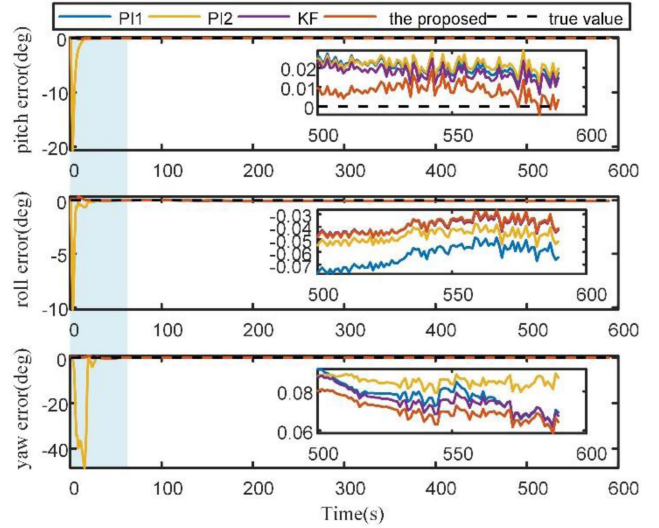


Fig. 18. Comparison of attitude error in field test.

V. CONCLUSION

Inertial-based integrated navigation using FGO technology has been popularized in the field of intelligent vehicles. However, little attention has been paid to the accuracy of preintegration models. The problems with traditional methods are:

- 1) The rotating earth is often ignored in the IMU preintegration, resulting in FGO being only applicable to low-precision IMUs.
- 2) The integration of the rotating earth is ignored, resulting in reduced attitude error.

This article focuses on the application of FGO in high-grade IMU. An exact IMU preintegration model is derived based on high-precision INS mechanization. It unifies the mathematical expressions for different precision levels of IMU, hence enabling the application of the FGO method more suitable for inertial-based integrated navigation with different precision IMUs. The method is compared against the state-of-the-art. Simulations and field tests show that the proposed method has obvious advantages in terms of the estimation accuracy of positioning and attitude. It broadens the application of FGO in inertial-based integrated navigation. In the future, FGO can be applied for long-term navigation, e.g., for autonomous underwater vehicles (AUV), and unmanned aerial vehicles equipped with high-grade inertial sensors. The interference of complex environment will be another challenge in the application of FGO method. Robust optimization methods will be the focus of further research in the future.

APPENDIX

A. Derivation of \mathbf{V}_j^n

According to (15), the velocity update equation from epoch $j-1$ to j is as follows.

$$\mathbf{V}_j^n = \mathbf{V}_{j-1}^n + \mathbf{C}_{ni}^{nj-1} \mathbf{C}_{bi}^{mi} \mathbf{C}_{bj-1}^{bi} \hat{\mathbf{f}}^{bj-1} \Delta t + \Delta \mathbf{V}_{cor/g(j-1)}^n \quad (35)$$

The velocity update equation from epoch $j-2$ to $j-1$ is as follows.

$$\mathbf{V}_{j-1}^n = \mathbf{V}_{j-2}^n + \mathbf{C}_{ni}^{nj-2} \mathbf{C}_{bi}^{bi} \mathbf{C}_{bj-2}^{bi} \hat{\mathbf{f}}^{bj-2} \Delta t + \Delta \mathbf{V}_{cor/g(j-2)}^n \quad (36)$$

Substitute (36) into (35) and iterate until \mathbf{V}_i^n . It can be obtained.

$$\begin{aligned} \mathbf{V}_j^n &= \mathbf{V}_{j-1}^n + \mathbf{C}_{ni}^{nj-1} \mathbf{C}_{bi}^{ni} \mathbf{C}_{bj-1}^{bi} \hat{\mathbf{f}}^{bj-1} \Delta t + \Delta \mathbf{V}_{cor/g(j-1)}^n \\ &= \mathbf{V}_{j-2}^n + \mathbf{C}_{ni}^{nj-2} \mathbf{C}_{bi}^{ni} \mathbf{C}_{bj-2}^{bi} \hat{\mathbf{f}}^{bj-2} \Delta t + \Delta \mathbf{V}_{cor/g(j-2)}^n \\ &\quad + \mathbf{C}_{ni}^{nj-1} \mathbf{C}_{bi}^{ni} \mathbf{C}_{bj-1}^{bi} \hat{\mathbf{f}}^{bj-1} \Delta t + \Delta \mathbf{V}_{cor/g(j-1)}^n \\ &= \dots \\ &= \mathbf{V}_i^n + \sum_{k=i}^{j-1} \mathbf{C}_{ni}^{nk} \mathbf{C}_{bi}^{ni} \mathbf{C}_{bk}^{bi} \hat{\mathbf{f}}^{bk} \Delta t + \Delta \mathbf{V}_{cor/g(ij)}^n \end{aligned} \quad (37)$$

B. Derivation of \mathbf{P}_j^n

According to (19), the position update equation from epoch $j-1$ to j is as follows.

$$\mathbf{P}_j^n = \mathbf{P}_{j-1}^n + \mathbf{V}_{j-1}^n \Delta t + \frac{1}{2} \mathbf{C}_{bj-1}^{nj-1} \hat{\mathbf{f}}^{bj-1} \Delta t^2 + \Delta \mathbf{P}_{cor/g(j-1)}^n \quad (38)$$

The position update equation from epoch $j-2$ to $j-1$ is as follows.

$$\mathbf{P}_{j-1}^n = \mathbf{P}_{j-2}^n + \mathbf{V}_{j-2}^n \Delta t + \frac{1}{2} \mathbf{C}_{bj-2}^{nj-2} \hat{\mathbf{f}}^{bj-2} \Delta t^2 + \Delta \mathbf{P}_{cor/g(j-2)}^n \quad (39)$$

Substitute (36), (39) into (38) and iterate until \mathbf{P}_i^n . It can be obtained.

$$\begin{aligned} \mathbf{P}_j^n &= \mathbf{P}_{j-1}^n + \mathbf{V}_{j-1}^n \Delta t + \frac{1}{2} \mathbf{C}_{bj-1}^{nj-1} \hat{\mathbf{f}}^{bj-1} \Delta t^2 + \Delta \mathbf{P}_{cor/g(j-1)}^n \\ &= \mathbf{P}_{j-2}^n + \mathbf{V}_{j-2}^n \Delta t + \frac{1}{2} \mathbf{C}_{bj-2}^{nj-2} \hat{\mathbf{f}}^{bj-2} \Delta t^2 + \Delta \mathbf{P}_{cor/g(j-2)}^n \\ &\quad + (\mathbf{V}_{j-2}^n + \mathbf{C}_{bj-2}^{nj-2} \hat{\mathbf{f}}^{bj-2} \Delta t + \Delta \mathbf{V}_{cor/g(j-2)}^n) \Delta t \\ &\quad + \frac{1}{2} \mathbf{C}_{bj-1}^{nj-1} \hat{\mathbf{f}}^{bj-1} \Delta t^2 + \Delta \mathbf{P}_{cor/g(j-1)}^n \\ &= \dots \\ &= \mathbf{P}_i^n + \mathbf{V}_i^n \Delta t_{i,j} + \frac{1}{2} \sum_{k=i}^{j-1} \mathbf{C}_{ni}^{nk} \mathbf{C}_{bi}^{ni} \mathbf{C}_{bk}^{bi} \hat{\mathbf{f}}^{bk} \Delta t^2 \\ &\quad + \sum_{k=i}^{j-2} \mathbf{C}_{ni}^{nk} \mathbf{C}_{bi}^{ni} \mathbf{C}_{bk}^{bi} \hat{\mathbf{f}}^{bk} \Delta t^2 + \Delta \mathbf{P}_{cor/g}^n \end{aligned} \quad (40)$$

C. Jacobians of Residual Errors

1) Jacobians of $r_{\mathbf{P}_{ij}}$: The Jacobian with respect to Φ_i is as follows

$$\begin{aligned} \frac{\partial r_{\mathbf{P}_{ij}}}{\partial \Phi_i} &= \frac{1}{2} \sum_{k=i}^{j-1} \mathbf{C}_{ni}^{nk} \mathbf{C}_{bi}^{ni} \left(\tilde{\mathbf{C}}_{bk}^{bi} \left(\hat{\mathbf{f}}^{bk} - \tilde{\mathbf{b}}_{ai} \right) \Delta t^2 \right) \times \\ &\quad + \sum_{k=i}^{j-2} \mathbf{C}_{ni}^{nk} \mathbf{C}_{bi}^{ni} \left(\tilde{\mathbf{C}}_{bk}^{bi} \left(\hat{\mathbf{f}}^{bk} - \tilde{\mathbf{b}}_{ai} \right) \Delta t^2 \right) \times \end{aligned}$$

$$\begin{aligned} &+ \frac{1}{2} \sum_{k=i}^{j-1} \mathbf{C}_{ni}^{nk} \mathbf{C}_{bi}^{ni} \left(\tilde{\mathbf{C}}_{bk}^{bi} \Delta t^2 \delta \mathbf{b}_{ai} \right) \times \\ &+ \sum_{k=i}^{j-2} \mathbf{C}_{ni}^{nk} \mathbf{C}_{bi}^{ni} \left(\tilde{\mathbf{C}}_{bk}^{bi} \Delta t^2 \delta \mathbf{b}_{ai} \right) \times \\ &+ \frac{1}{2} \sum_{k=i}^{j-1} \mathbf{C}_{ni}^{nk} \mathbf{C}_{bi}^{ni} \left(\tilde{\mathbf{C}}_{bk}^{bi} \left(\hat{\mathbf{f}}^{bk} - \tilde{\mathbf{b}}_{ai} \right) \times \frac{\partial \tilde{\mathbf{C}}_{bk}^{bi}}{\partial \tilde{\mathbf{b}}_{gi}} \Delta t^2 \delta \mathbf{b}_{gi} \right) \times \\ &+ \sum_{k=i}^{j-2} \mathbf{C}_{ni}^{nk} \mathbf{C}_{bi}^{ni} \tilde{\mathbf{C}}_{bk}^{bi} \left(\left(\hat{\mathbf{f}}^{bk} - \tilde{\mathbf{b}}_{ai} \right) \times \frac{\partial \tilde{\mathbf{C}}_{bk}^{bi}}{\partial \tilde{\mathbf{b}}_{gi}} \Delta t^2 \delta \mathbf{b}_{gi} \right) \times \end{aligned} \quad (41)$$

The Jacobians with respect to the rest of states are as follows

$$\begin{aligned} \frac{\partial r_{\mathbf{P}_{ij}}}{\partial p_j} &= -\mathbf{C}_{bi}^{nj} \frac{\partial r_{\mathbf{P}_{ij}}}{\partial p_j} = -\mathbf{C}_{bj}^{nj} \\ \frac{\partial r_{\mathbf{P}_{ij}}}{\partial v_i} &= -\mathbf{I}_3 \Delta t_{i,j} + \frac{1}{2} \Delta t_{i,j}^2 (2\omega_{ie}^n + \omega_{en}^n) \times \\ \frac{\partial r_{\mathbf{P}_{ij}}}{\partial v_j} &= 0_3 \frac{\partial r_{\mathbf{P}_{ij}}}{\partial \Phi_j} = 0_3 \\ \frac{\partial r_{\mathbf{P}_{ij}}}{\partial \delta \mathbf{b}_{ai}} &= -\mathbf{L}_2 \frac{\partial r_{\mathbf{P}_{ij}}}{\partial \delta \mathbf{b}_{gi}} = -\mathbf{L}_3 \end{aligned} \quad (42)$$

2) Jacobians of $r_{\mathbf{V}_{ij}}$: The Jacobian with respect to Φ_i is as follows

$$\begin{aligned} \frac{\partial r_{\mathbf{V}_{ij}}}{\partial \Phi_i} &= \frac{\partial r_{\mathbf{V}_{ij}}}{\partial \Phi_i} \\ &= \sum_{k=i}^{j-1} \mathbf{C}_{ni}^{nk} \mathbf{C}_{bi}^{ni} \left(\tilde{\mathbf{C}}_{bk}^{bi} \left(\hat{\mathbf{f}}^{bk} - \tilde{\mathbf{b}}_{ai} \right) \Delta t \right) \times \\ &\quad + \sum_{k=i}^{j-1} \mathbf{C}_{ni}^{nk} \mathbf{C}_{bi}^{ni} \left(\tilde{\mathbf{C}}_{bk}^{bi} \Delta t \delta \mathbf{b}_{ai} \right) \times \\ &\quad + \sum_{k=i}^{j-1} \mathbf{C}_{ni}^{nk} \mathbf{C}_{bi}^{ni} \left(\tilde{\mathbf{C}}_{bk}^{bi} \left(\hat{\mathbf{f}}^{bk} - \tilde{\mathbf{b}}_{ai} \right) \times \frac{\partial \tilde{\mathbf{C}}_{bk}^{bi}}{\partial \tilde{\mathbf{b}}_{gi}} \Delta t \delta \mathbf{b}_{gi} \right) \times \end{aligned} \quad (43)$$

The Jacobians with respect to the rest of states are as follows

$$\begin{aligned} \frac{\partial r_{\mathbf{V}_{ij}}}{\partial p_i} &= 0_3 \frac{\partial r_{\mathbf{P}_{ij}}}{\partial p_j} = 0_3 \\ \frac{\partial r_{\mathbf{P}_{ij}}}{\partial v_i} &= -\mathbf{I}_3 + (2\omega_{ie}^n + \omega_{en}^n) \times \Delta t_{i,j} \\ \frac{\partial r_{\mathbf{P}_{ij}}}{\partial v_j} &= \mathbf{I}_3 \frac{\partial r_{\mathbf{P}_{ij}}}{\partial \Phi_j} = 0_3 \\ \frac{\partial r_{\mathbf{P}_{ij}}}{\partial \delta \mathbf{b}_{ai}} &= -\sum_{k=i}^{j-1} \mathbf{C}_{ni}^{nk} \mathbf{C}_{bi}^{ni} \tilde{\mathbf{C}}_{bk}^{bi} \Delta t \\ \frac{\partial r_{\mathbf{P}_{ij}}}{\partial \delta \mathbf{b}_{gi}} &= -\sum_{k=i}^{j-1} \mathbf{C}_{ni}^{nk} \mathbf{C}_{bi}^{ni} \tilde{\mathbf{C}}_{bk}^{bi} \left(\hat{\mathbf{f}}^{bk} - \tilde{\mathbf{b}}_{ai} \right) \times \frac{\partial \tilde{\mathbf{C}}_{bk}^{bi}}{\partial \tilde{\mathbf{b}}_{gi}} \Delta t \end{aligned} \quad (44)$$

3) *Jacobians of $r_{C_{bj}^{bi}}$:* The Jacobian with respect to Φ_i is as follows

$$\frac{\partial r_{C_{bj}^{bi}}}{\partial \Phi_i} = -\mathbf{J}_r^{-1} \left(r_{C_{bj}^{bi}} (\mathbf{C}_{bi}^{ni}) \right) \left(\mathbf{C}_{bj}^{nj} \right)^T \mathbf{C}_{ni}^{nj} \mathbf{C}_{bi}^{ni} \quad (45)$$

where $\mathbf{J}_r^{-1}(r_{C_{bj}^{bi}}(\mathbf{C}_{bi}^{ni}))$ is the inverse of the right Jacobian $\mathbf{J}_r(r_{C_{bj}^{bi}}(\mathbf{C}_{bi}^{ni}))$.

The Jacobians with respect to the rest of states are as follows

$$\frac{\partial r_{C_{bj}^{bi}}}{\partial p_i} = \mathbf{0}_3 \frac{\partial r_{C_{bj}^{bi}}}{\partial p_j} = \mathbf{0}_3 \frac{\partial r_{C_{bj}^{bi}}}{\partial \delta \mathbf{b}_{ai}} = \mathbf{0}_3$$

$$\frac{\partial r_{C_{bj}^{bi}}}{\partial \Phi_j} = \mathbf{J}_r^{-1} \left(r_{C_{bj}^{bi}} (\mathbf{C}_{bj}^{nj}) \right)$$

$$\frac{\partial r_{C_{bj}^{bi}}}{\partial v_i} = \mathbf{0}_3 \frac{\partial r_{C_{bj}^{bi}}}{\partial v_j} = \mathbf{0}_3$$

$$\frac{\partial r_{C_{bj}^{bi}}}{\partial \delta \mathbf{b}_{gi}} = -\mathbf{J}_r^{-1} \left(r_{C_{bj}^{bi}} (\delta \mathbf{b}_{gi}) \right) \text{Exp} \left(r_{C_{bj}^{bi}} (\delta \mathbf{b}_{gi}) \right)^T \mathbf{J}_r^b \frac{\partial \tilde{\mathbf{C}}_{bj}^{bi}}{\partial \tilde{\mathbf{b}}_{gi}} \quad (46)$$

where $\mathbf{J}_r^b = \mathbf{J}_r \left(\frac{\partial \tilde{\mathbf{C}}_{bj}^{bi}}{\partial \tilde{\mathbf{b}}_{gi}} \delta \mathbf{b}_{gi} \right)$.

REFERENCES

- [1] W. Liu, K. Quijano, and M. M. Crawford, “YOLOv5-tassel: Detecting tassels in RGB UAV imagery with improved YOLOv5 based on transfer learning,” *IEEE J. Sel. Topics Appl. Earth Observ. Remote Sens.*, vol. 15, pp. 8085–8094, 2022.
- [2] X. Xia et al., “Automated driving systems data acquisition and processing platform,” *Transp. Res. Part C: Emerg. Technol.*, vol. 151, 2023, Art. no. 104120.
- [3] K. Takeyama, T. Machida, Y. Kojima, and N. Kubo, “Improvement of dead reckoning in urban areas through integration of low-cost multisensors,” *IEEE Trans. Intell. Veh.*, vol. 2, no. 4, pp. 278–287, Dec. 2017.
- [4] B. Barshan and H. Durrant-Whyte, “Inertial navigation systems for mobile robots,” *IEEE Robot. Automat. Soc.*, vol. 11, no. 3, pp. 328–342, Jun. 1995.
- [5] M. Zhong, J. Guo, and D. Zhou, “Adaptive In-flight alignment of INS/GPS systems for aerial mapping,” *IEEE Trans. Aerosp. Electron. Syst.*, vol. 54, no. 3, pp. 1184–1196, Jun. 2018.
- [6] N. Souli, P. Kolios, and G. Ellinas, “Online relative positioning of autonomous vehicles using signals of opportunity,” *IEEE Trans. Intell. Veh.*, vol. 7, no. 4, pp. 873–885, Dec. 2022.
- [7] M. Ramezani and K. Khoshelham, “Vehicle positioning in GNSS-deprived urban areas by stereo visual-inertial odometry,” *IEEE Trans. Intell. Veh.*, vol. 3, no. 2, pp. 208–217, Jun. 2018.
- [8] C. Shen et al., “Seamless GPS/inertial navigation system based on self-learning square-root cubature Kalman filter,” *IEEE Trans. Ind. Electron.*, vol. 68, no. 1, pp. 499–508, Jan. 2021.
- [9] X. Xia, E. Hashemi, L. Xiong, A. Khajepour, and N. Xu, “Autonomous vehicles sideslip angle estimation: Single antenna GNSS/IMU fusion with observability analysis,” *IEEE Internet Things J.*, vol. 8, no. 19, pp. 14845–14859, Oct. 2021.
- [10] X. Xia, E. Hashemi, L. Xiong, and A. Khajepour, “Autonomous vehicle kinematics and dynamics synthesis for sideslip angle estimation based on consensus Kalman filter,” *IEEE Trans. Control Syst. Technol.*, vol. 31, no. 1, pp. 179–192, Jan. 2023.
- [11] K. L. Lim et al., “Evolution of a reliable and extensible high-level control system for an autonomous car,” *IEEE Trans. Intell. Veh.*, vol. 4, no. 3, pp. 396–405, Sep. 2019.
- [12] A. Brunker, T. Wohlgemuth, M. Frey, and F. Gauterin, “Odometry 2.0: A slip-adaptive EIF-based four-wheel-odometry model for parking,” *IEEE Trans. Intell. Veh.*, vol. 4, no. 1, pp. 114–126, Mar. 2019.
- [13] L. Li, M. Yang, H. Li, C. Wang, and B. Wang, “Robust localization for intelligent vehicles based on compressed road scene map in urban environments,” *IEEE Trans. Intell. Veh.*, vol. 8, no. 1, pp. 250–262, Jan. 2023.
- [14] G. Guo and S. Zhao, “3D multi-object tracking with adaptive cubature Kalman filter for autonomous driving,” *IEEE Trans. Intell. Veh.*, vol. 8, no. 1, pp. 512–519, Jan. 2023.
- [15] D. Yuan, Y. Qin, Z. Wu, and X. Shen, “A robust multi-state constraint optimization-based orientation estimation system for Satcom-on-the-move,” *IEEE Trans. Instrum. Meas.*, vol. 70, 2021, Art. no. 5503314.
- [16] N. Sünderhauf and P. Protzel, “Towards robust graphical models for GNSS-based localization in urban environments,” in *Proc. Int. Multi-Conf. Syst., Signals Devices*, 2012, pp. 1–6.
- [17] G. Zhang, H.-F. Ng, W. Wen, and L.-T. Hsu, “3D mapping database aided GNSS based collaborative positioning using factor graph optimization,” *IEEE Trans. Intell. Transp. Syst.*, vol. 22, no. 10, pp. 6175–6187, Oct. 2021.
- [18] W. W. Wen and L.-T. Hsu, “3D LiDAR aided GNSS NLOS mitigation in urban canyons,” *IEEE Trans. Intell. Transp. Syst.*, vol. 23, no. 10, pp. 18224–18236, Oct. 2022.
- [19] C. Forster, L. Carbone, F. Dellaert, and D. Scaramuzza, “On-manifold preintegration for real-time visual-inertial odometry,” *IEEE Trans. Robot.*, vol. 33, no. 1, pp. 1–21, Feb. 2017.
- [20] T. Qin, P. Li, and S. Shen, “VINS-mono: A robust and versatile monocular visual-inertial state estimator,” *IEEE Trans. Robot.*, vol. 34, no. 4, pp. 1004–1020, Aug. 2018.
- [21] T. Shan, B. Englot, D. Meyers, W. Wang, C. Ratti, and D. Rus, “LIO-SAM: Tightly-coupled lidar inertial odometry via smoothing and mapping,” in *Proc. IEEE/RSJ Int. Conf. Intell. Robots Syst.*, 2020, pp. 5135–5142.
- [22] W. Wen, T. Pfeifer, X. Bai, and L. - T. Hsu, “Factor graph optimization for GNSS/INS integration: A comparison with the extended Kalman filter,” *Navigation*, vol. 68, no. 2, pp. 315–331, 2021.
- [23] J. Henawy, Z. Li, W.-Y. Yau, and G. Seet, “Accurate IMU factor using switched linear systems for VIO,” *IEEE Trans. Ind. Electron.*, vol. 68, no. 8, pp. 7199–7208, Aug. 2021.
- [24] K. Eckenhoff, P. Geneva, and G. Huang, “Closed-form preintegration methods for graph-based visual-Inertial navigation,” *Int. J. Robot. Res.*, vol. 38, no. 5, pp. 563–586, 2019.
- [25] S. Bai, J. Lai, P. Lyu, Y. Cen, and B. Ji, “Improved preintegration method for GNSS/IMU/in-vehicle sensors navigation using graph optimization,” *IEEE Trans. Veh. Technol.*, vol. 70, no. 11, pp. 11446–11457, Nov. 2021.
- [26] M. Brossard, A. Barrau, P. Chauchat, and S. Bonnabel, “Associating uncertainty to extended poses for on lie group IMU preintegration with rotating earth,” *IEEE Trans. Robot.*, vol. 38, no. 2, pp. 998–1015, Apr. 2022.
- [27] H. Tang, T. Zhang, X. Niu, J. Fan, and J. Liu, “Impact of the earth rotation compensation on MEMS-IMU preintegration of factor graph optimization,” *IEEE Sensors J.*, vol. 22, no. 17, pp. 17194–17204, Sep. 2022.
- [28] J. Ding, C. Huang, J. Cheng, F. Wang, and Y. Hu, “Refined on-manifold IMU preintegration theory for factor graph optimization based on equivalent rotation vector,” *IEEE Sensors J.*, vol. 23, no. 5, pp. 5200–5219, Mar. 2023.
- [29] L. Zhang, L.-T. Hsu, and T. Zhang, “A novel INS/USBL integrated navigation scheme via factor graph optimization,” *IEEE Trans. Veh. Technol.*, vol. 71, no. 9, pp. 9239–9249, Sep. 2022, doi: [10.1109/TVT.2022.3177739](https://doi.org/10.1109/TVT.2022.3177739).
- [30] Z. Zhang, J. Zhao, C. Huang, and L. Li, “Learning visual semantic map-matching for loosely multi-sensor fusion localization of autonomous vehicles,” *IEEE Trans. Intell. Veh.*, vol. 8, no. 1, pp. 358–367, Jan. 2023.
- [31] M. Ramezani and K. Khoshelham, “Vehicle positioning in GNSS-deprived urban areas by stereo visual-inertial odometry,” *IEEE Trans. Intell. Veh.*, vol. 3, no. 2, pp. 208–217, Jun. 2018..
- [32] M. Brossard, A. Barrau, and S. Bonnabel, “AI-IMU dead-reckoning,” *IEEE Trans. Intell. Veh.*, vol. 5, no. 4, pp. 585–595, Dec. 2020.
- [33] L. Zhang, T. Zhang, M. Wang, J. Wang, and Y. Li, “A high-order coning error compensation algorithm under high rate maneuvering,” *IEEE Sensors J.*, vol. 20, no. 1, pp. 208–218, Jan. 2020.
- [34] P. Savage, “Strapdown inertial navigation integration algorithm design part 2: Velocity and position algorithms,” *AIAA J. Guid., Control, Dyn.*, vol. 21, no. 2, pp. 208–221, Mar./Apr. 1998.
- [35] M. Moakher, “Means and averaging in the group of rotations,” *SIAM J. Matrix Anal. Appl.*, vol. 24, no. 1, pp. 1–16, 2002.
- [36] L. Chang, J. Di, and F. Qin, “Inertial-based integration with transformed INS mechanization in earth frame,” *IEEE/ASME Trans. Mechatronics*, vol. 27, no. 3, pp. 1738–1749, Jun. 2022.
- [37] Y. Gao, Y. Jiang, and G. Huang, “A linear Kalman filter-based integrity monitoring considering colored measurement noise,” *GPS Solutions*, vol. 25, no. 2, pp. 1–13, 2021.
- [38] Y. Huang, Y. Zhang, N. Li, Z. Wu, and J. A. Chambers, “A novel robust student’s T-based Kalman filter,” *IEEE Trans. Aerosp. Electron. Syst.*, vol. 53, no. 3, pp. 1545–1554, Jun. 2017.



Liang Zhang (Member, IEEE) received the Ph.D. degree from Instruments Science and Technology, Southeast University, Nanjing, China, in 2021, and the M.S. degree in navigation, guidance, and control from the Nanjing University of Aeronautics and Astronautics, Nanjing, China, in 2017. He was a Postdoctoral Fellow with the Department of Aeronautical and Aviation Engineering, Hong Kong Polytechnic University, Hong Kong, in 2022. He is currently a Lecturer with the School of Instrument Science and Engineering, Southeast University. His research interest includes inertial navigation, integrated navigation technology, and underwater positioning technology.



Li-Ta Hsu (Senior Member, IEEE) received the B.S. and Ph.D. degrees in aeronautics and astronautics from the National Cheng Kung University, Taiwan, in 2007 and 2013, respectively. He is currently an Associate Professor with the Department of Aeronautical and Aviation Engineering, Hong Kong Polytechnic University, Hong Kong. He is also Limin Endowed Young Scholar of aerospace navigation. He was a Visiting Researcher with the Faculty of Engineering, University College London, London, U.K., and the Tokyo University of Marine Science and Technology, Tokyo, Japan, in 2012 and 2013, respectively. From 2014 to 2016, he was selected as a JSPS Postdoctoral Fellow with The University of Tokyo, Tokyo, Japan. He is also an Associate Fellow with the Royal Institute of Navigation, London, U.K. He is the Members of Institute of Navigation (ION) and IEEE and is the Member of the editorial board and reviewer in professional journals related to navigation and GNSS.



Weisong Wen received the Ph.D. degree in mechanical engineering from Hong Kong Polytechnic University, Hong Kong. He was a Visiting Student Researcher with the University of California, Berkeley, CA, USA, in 2018. He is currently a Research Assistant Professor with the Department of Aeronautical and Aviation Engineering, Hong Kong Polytechnic University.

His research interests include multi-sensor integrated localization for autonomous vehicles, SLAM, and GNSS positioning in urban canyons.



Tao Zhang received the Ph.D. degree in precision instrument and machinery from Southeast University, Nanjing, China, in 2008. He is currently a Professor with the School of Instrument Science and Engineering, Southeast University, Nanjing, China. His research interests include inertial navigation, AUV underwater positioning, and integrated navigation.